Journal Pre-proof

Electrically controlled interface state distribution for improving pyro-phototronic photosensing from UV to NIR

Meng Zhu, Xianchun Qiu, Jiayao Liu, Qing Chang, Zhaona Wang, Zhong Lin Wang

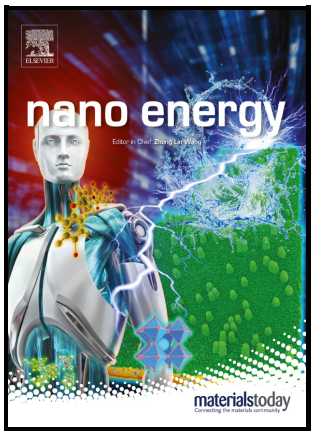

PII: S2211-2855(25)00259-9

DOI: https://doi.org/10.1016/j.nanoen.2025.110900

Reference: NANOEN110900

To appear in: *Nano Energy*

Received date: 8 February 2025
Revised date: 7 March 2025
Accepted date: 18 March 2025

Please cite this article as: Meng Zhu, Xianchun Qiu, Jiayao Liu, Qing Chang, Zhaona Wang and Zhong Lin Wang, Electrically controlled interface state distribution for improving pyro-phototronic photosensing from UV to NIR, *Nano Energy,* (2025) doi:https://doi.org/10.1016/j.nanoen.2025.110900

Electrically controlled interface state distribution for improving pyro-phototronic photosensing from UV to NIR

Meng Zhu[1], Xianchun Qiu[1], Jiayao Liu[1], Qing Chang[2], Zhaona Wang[1,*] and Zhong Lin Wang[3,*]

[1]Applied Optics Beijing Area Major Laboratory, Key Laboratory of Multiscale Spin Physics (Ministry of Education), School of Physics and Astronomy, Beijing Normal University, Beijing 100875, P. R. China

[2]College of Arts and Sciences, Beijing Normal University at Zhuhai, Zhuhai 519087, P. R. China.

[3]School of Materials Science and Engineering, Georgia Institute of Technology, Atlanta, GA 30332, USA

[4]Beijing Institute of Nanoenergy and Nanosystems, Chinese Academy of Sciences, Beijing 100083, P. R. China

e-mail: zhnwang@bnu.edu.cn，zlwang@binn.cas.cn

Abstract

The interface states (ISs) in oxide semiconductor have long been considered a key factor for limiting the photoresponse performance of oxide-based photodetectors (PDs). Here, the IS distribution is electrically tailored and proposed as an effective strategy to improve the performances of the ZnO-based PDs. A graded IS (GIS) with tunable gradient is achieved through an electric field-assisted UV irradiation to significantly enhance the built-in electric field of the heterojunction. The corresponding steady (transient) photocurrent responsivity of the heterojunction as a self-powered PD is thus improved by a maximal factor of 1540% (237%) relative to the junction under the initial IS condition for 320-1120 nm waves. More importantly, the tunable IS distribution can modulate pyro-phototronic effect. This work provides an effective approach to manipulate IS distribution in oxide semiconductor and a potential perspective on using disorder IS to design the self-powered PDs.

Keywords

interface state, graded interface state, pyro-phototronic effect, self-powered photodetector

Introduction

Currently, self-powered photodetectors (PDs)[1-3] based on photovoltaic (PV) effect have garnered significant application potentials due to their advantages of low dark current, large build-in electric filed and free from external power sources. Among them, various of p-Si/n-ZnO heterojunctions have been investigated as a self-powered PD due to simple fabrication, ease of integration, environmentally friendly, and broad band optical responses.[4-10] Particularly, nanoscale ZnO materials are primarily used as photoactive layers or electron transport layers to achieve photoelectric conversion. Various optimization strategies[11-15] such as morphology and dimension control,[16-19] doping,[20-22] and energy-band engineering[23-26] have been proposed to modify the physical property of the nanoscale ZnO materials and ZnO-based junctions. The photoelectric response performances of the ZnO-based PDs have been greatly improved.[27-30] However, abundant recombining centers induced by the inherent surface electronic state of the oxide semiconductor[31-36] still distribute randomly within the amorphous, even crystal films fabricated through various methods, and greatly affect and limit the detection performances of the ZnO-based PDs. To eliminate the surface or interface state (IS) within ZnO material, the researchers have explored several types of physical or/and chemical modification strategies, such as hydrogenation,[37] surface passivation,[38] thermal treatment,[39] ion implantation[40] and optical irradiation.[13] Particularly, ultraviolet (UV) irradiation is a flexible and effective approach to reduce the IS concentration within the ZnO nanowires, leading to a huge improvement in photoresponsivity of the p-Si/n-ZnO self-powered PD.[13] These works mainly concerned on decreasing the IS average concentration within the ZnO layer to improve the performances of the ZnO-based PDs through building up the p-n junction model with IS located at the interface. Considering the charge property of the IS, IS distribution will result in the spatial charge distribution in the oxide semiconductor. The introduced spatial charge will modify the built-in field and transportation of the photo-generated carriers, and then affect the optoelectrical property of p-n heterojunction. Thus, it is necessary to investigate the modification role

of the IS distribution on the optoelectrical property of p-n junction as a self-powered PD.

For the self-powered PDs with p-n junction, polarization field-related interfacial physical effects have also been proposed to significantly enhance their photon detecting ability and uncover the fascinating photovoltaic phenomena during the photoelectric conversion process.[10, 41-43] In particular, pyro-phototronic effect[42] has been proposed as a promising interfacial physical effect to boost the response performances of the self-powered PDs by coupling the light-induced pyroelectric effect and photovoltaic effect. The light-induced pyroelectric polarization charges can effectively promote local carriers' separation and transportation in the p-n junction.[44, 45] Moreover, the broadband property of pyroelectric effect induced by light-disturbing offer an ideal platform for achieving broadband response beyond the energy bandgap.[46-48] The photocurrent response speed, responsivity and spectral bandwidth of the self-powered PDs are thus significantly improved by the pyro-phototronic effect.[2, 49] Moreover, a series of physical parameters such as bias voltage,[50] environment temperature,[51] chopping frequency,[52] and IS concentration[13] have been tuned to improve the performances of the pyro-phototronic PDs. The coupling role of pyro-phototronic effect with other physical effects[53, 54] have also been investigated to optimize the pyro-phototronic PDs. In particular, decreasing IS concentration through UV irradiation as a non-contact approach has significant enhancement role on the pyro-phototronic effect.[13] However, the impact of the IS concentration distribution on pyro-phototronic effect is still an important but open question considering that the pyroelectric polarization charge is highly susceptible to the IS or defects due to the depolarization.[9] Therefore, it is significant to thoroughly investigate and utilize concentration gradient of random-distribution IS to tailor pyro-phototronic effect for designing the high-performance PDs.

Here, a GIS with tunable gradient is proposed and achieved through a smart approach of external electric field-assisted UV irradiation within ZnO nanofilm with plenty of grains. The introduced GIS within ZnO nanofilm significantly enlarges the built-in potential and improves the photocurrent response of the p-n junction. By

coupling pyro-phototronic effect, the heterojunction with GIS demonstrates the excellent response performances over a broad band from 320 to 1120 nm as a self-powered PD. The stable photocurrent of the PD with the GIS is maximally improved by 1540% (486%) relative to the case with initial IS (low concentration IS, LCIS). The transient peak-to-peak photocurrent is also improved by a factor of about 237% (154%) relative to the self-powered PD with IIS (LCIS), indicating an enhancement role of GIS (IS concentration gradient) on pyro-phototronic effect. More importantly, the concentration and gradient of the IS can be flexibly modulated by adjusting the UV irradiation energy density and external electric field intensity. Moreover, this proposed GIS generation method can be extended to other oxide-based p-n junctions, providing a flexible and effective approach to manipulate the concentration gradient of random-distributed IS in oxide semiconductor films for designing high-performance PDs.

Results

Tailoring principle of IS distribution. Generally, the ZnO nanofilm fabricated by chemical method contains a considerable amount of negative oxygen ions (O_2^-) at the interface of the grains, meaning abundant random-distribution IS with statistically uniform distribution within ZnO. This condition is named as initial IS (IIS) shown in Fig. 1a(i). The ZnO with IIS has a relatively low level of electron concentration due to the capture of the ISs. When the ZnO nanofilm is exposed to 325 nm UV lasing, the photo-generated holes by UV irradiation can combine with O_2^- to generate O_2 molecules spreading to the environment through the interface.[31] As a result, the concentration of O_2^- is greatly reduced and a uniform distribution of IS with a low concentration is obtained as the LCIS (Fig. 1a(ii)). Accordingly, decrease of IS concentration results in a proportional escalation of the electron concentration within the ZnO nanofilm. To tailor the IS concentration distribution, an external electric field is introduced to manipulate the irradiation-induced hole distribution (Fig. 1a(iii)). The modified hole distribution will further induce the IS distribution along the direction of the treated electric field $\boldsymbol{E}_{tr}$, ultimately reaching an equilibrium state. In regions with high hole concentration, large portion of O_2^- is turned into O_2, whereas in areas with lower hole concentration, only a small amount of O_2^- is released. Consequently, the O_2^-

concentration within the ZnO nanofilm is reduced and distributed nonuniformly along the $\boldsymbol{E}_{tr}$ direction (Fig. 1a(iii)). This results in a decrease in the average IS concentration and establishes a reverse IS concentration gradient relative to the $\boldsymbol{E}_{tr}$ direction, thereby forming the GIS state. Therefore, the application of an external electric field is critical for achieving gradient-distributed IS and controlling the direction of the IS concentration gradient. The corresponding ZnO film with a high electron concentration and a gradient IS distribution can be obtained through the process of electric field-assisted UV irradiation. This is the fundamental principle of tailoring the IS distribution in ZnO nanofilm.

Design mechanism of GIS-improved PDs. To uncover the tuning role of GIS on transportation of p-n junction, a physical model of unilateral depletion p-n junction with tunable average electron concentration and spatial charges within the depleted ZnO nanofilm is constructed.[53-55] In this model, IS average concentration tailors the electron concentration within the ZnO film as mentioned above. At the same time, the IS induced by O_2^- at the interfaces will lead to the screening charges in the adjacent area and the corresponding induced charges within a grain of ZnO nanocrystals, being equivalently as the dipoles. For the film with random-distribution IS, the equivalent dipoles are random in direction and uniform in space, meaning none net spatial charge distribution in ZnO. For the ZnO film under the GIS condition, the equivalent dipoles are nonuniformly distributed along the assisted $\boldsymbol{E}_{tr}$ direction and tend to align opposite to the IS concentration gradient. Considering the cumulative effect of each nanolayer, uniformly distributed negative net charges are induced within the fully depleted ZnO film, while corresponding positive net charges are generated at the outer surface (Fig. S1, supporting information). As a result, a p-n junction model with spatially distributed polarization charges is constructed as shown in Fig.1b(i) for the p-Si/n-ZnO with GIS. The additional electric field (E_{GIS}) induced by the distributed net charges aligns with the intrinsic built-in electric field (E_{bi}) of the p-n junction, resulting in a significant improvement of the total built-in electric field. A larger built-in electric field and potential are clearly observed in the p-Si/n-ZnO heterojunction with GIS, compared to the heterojunction under the IIS and LCIS conditions, as investigated in Fig. 1b (ii, iii)

and S2 (supporting information). This enhanced equivalent built-in electric field not only promotes the separation and transportation of the photogenerated carriers but also facilitates the regulation of pyro-phototronic effect.[48] Additionally, the polarization field generated by the GIS, aligned with built-in electric field, leads to a distinctly tilted energy band within the ZnO side, further improving carrier migration efficiency (Fig. S3). Consequently, the photoelectric response performances of the p-Si/n-ZnO heterojunction is significantly improved by the GIS as a self-powered PD. This outlines the design principle of the GIS-improved PD based on oxide semiconductor.

In our experiments, a p-Si/n-ZnO heterojunction is fabricated by spin-coating a ZnO precursor solution onto a cleaned silicon substrate using the sol-gel method.[48] Top-view and side view scanning electron microscopy (SEM) images of the heterojunction reveal that the ZnO nanofilm, as shown in Fig. 1c, consists of numerous grain boundaries and has a thickness of approximately 100 nm. The IS distribution within the ZnO layer of the p-Si/n-ZnO junction is further modified via the treatment technique of electric field-assisted UV irradiation. In this process, a 325 nm laser is used as an irradiation source to reduce the average IS concentration within ZnO film, while the treatment electric field $\boldsymbol{E}_{tr}$, supplied by a DC power, is applied to generate and modify IS concentration gradient within ZnO film, as illustrated in Fig. 1d. Consequently, the GIS distribution within the ZnO nanofilm can be achieved and tuned by controlling the UV irradiation energy density and the applying $\boldsymbol{E}_{tr}$ intensity. To clarify the treating electric field ($\boldsymbol{E}_{tr}$) in the ZnO, the partial voltage U_{ZnO} of the external bias U_{ex} on the ZnO film is estimated based on the transportation model of the p-n junction (Fig. S4, supporting information). Using this technique, the treated p-Si/n-ZnO junction with tunable GIS is obtained (Fig. 1e), exhibiting an increasing IS concentration from the interface to the top surface. To demonstrate the modification role of the applying $\boldsymbol{E}_{tr}$ on IS distribution, the electric field-assisted UV irradiation is utilized to modify the lateral gradient of IS distribution in a pure ZnO film on a quartz substrate, as depicted in Fig. S5a (supporting information). Local photoluminescence (PL) and transient absorption (TA) spectra are measured along the direction of the treating electric field $\boldsymbol{E}_{tr}$ on the ZnO film, revealing the nonuniform distribution of the

IS in ZnO film. The PL integral intensity and the relative ratio of the defect peak in the visible region to the intrinsic emission peak both exhibit a gradual decrease from region #1 to region #3 (Fig. 1f and Fig. S5b, supporting information), indicating a reduction in IS concentration along the direction of $\boldsymbol{E}_{tr}$.[13] Additionally, the carrier lifetime of the fast decay process obtained from TA spectra increases along $\boldsymbol{E}_{tr}$ direction (Fig. S5c, supporting information), further confirming the decrease in IS concentration.[56-58] The result demonstrates a lateral gradient of IS distribution in the ZnO film along the $\boldsymbol{E}_{tr}$ direction via electric field-assisted UV irradiation. It also tells us that a vertical treating electric field during UV irradiation will introduce a vertical gradient of IS distribution, which is align with the built-in field of the p-n junction. Thus, a vertical electric field-assisted UV irradiation is used to modify the vertical distribution of the IS and achieve the GIS along the p-n junction direction in our experiments.

The tuning role of GIS on the electric transport of the p-Si/n-ZnO junction is also characterized under the vacuum chamber supplying an oxygen-less environment (Fig. S6a, supporting information). The Nyquist plots of the p-n junction with different IS distributions are presented in Fig. 1g. The interface charge transport resistance (R_{ct}) of the junction under the GIS condition is lower than those of the junction under the IIS and LCIS conditions (Table S1, supporting information), indicating that the obtained IS concentration gradient facilitates electron transfer through the p-Si/n-ZnO interface. The corresponding measured built-in potential of the heterojunctions, the donor concentration in ZnO and interface charge amount are acquired through capacitance-voltage (C^{-2}-V) curves of the p-n junction with IS [59, 60] in Fig. 1h based on the unilateral depletion junction model with the following relation:

$$C^{-2} = \left(\frac{q\varepsilon_1\varepsilon_2 N_1 N_2}{2(\varepsilon_1 N_1 + \varepsilon_2 N_2)}\right)^{-1}\left(V_{bi} - V - \frac{Q_{IS}^2}{2q(\varepsilon_1 N_1 + \varepsilon_2 N_2)}\right) \qquad (1)$$

Where Q_{IS} is the interface charge per unit area, V_{bi} is the built-in potential of the ideal p-n junction without IS, N is the ionized impurity density, and ε is the dielectric constant. The subscripts 1and 2 denote the two sides of the junction. The heterojunction under the GIS condition demonstrates a largest measured built-in potential of 0.48 V relative to the junction under the IIS condition and under the LCIS condition as simulated above.

The large built-in potential indicates that the obtained GIS can provide a strong driving force for carrier separation and transport for a self-powered PD. The donor doping concentration of the ZnO film under the GIS (LCIS) condition is further calculated as 1.67×10^{17} m^{-3} (1.66×10^{17} m^{-3}), slightly higher than that (1.6×10^{17} m^{-3}) of the initial film (IIS). This increase in carrier concentration can be attributed to the decrease of IS concentration as analyzed above. Additionally, based on the difference (ΔV) of the measured built-in potential between the p-n junction with GIS and the junction with IIS, one can directly determine the $\Delta Q_{IS}{}^2$ with the following relation:

$$\Delta Q_{IS}{}^2 = -(2q\Delta V(\varepsilon_1 N_1 + \varepsilon_2 N_2)) \quad (2)$$

Considering that the IS concentration of the heterojunction with GIS condition is significantly reduced relative to the initial IS, then decrease in interface charge can be estimated by the following relation:

$$\Delta Q_{IS} \approx -(2q\Delta V(\varepsilon_1 N_1 + \varepsilon_2 N_2))^{1/2} \quad (3)$$

Based on the variation of the measured built-in potential, the corresponding interface charge can be calculated. The built-in potential increases by 0.16 V after forming the GIS. The corresponding IS concentration ΔQ_{IS} per unit area decreased by 5.7×10^{-5} C m^{-2}. Assuming each IS possessing a unit charge, the IS density is reduced by 3.6×10^{10} cm^{-2}. This may provide valuable evidence for the electrical property of graded IS modulation. The *I-V* curve of p-Si/n-ZnO junction under the GIS condition (Fig. S6b, supporting information) shows a larger rectification ratio relative to those of the junction under the IIS and LCIS conditions, demonstrating a better electric transport performance. This GIS-enhanced electric transport of the p-Si/n-ZnO junction is benefit to fabricate a self-powered sensor with outstanding performances.

General performances of the GIS-improved PDs. The enhancement effect of the obtained GIS on the photon response performances of the self-powed PD is carefully displayed through comparing the transient photon current response of the p-Si/n-ZnO junction under the IIS, LCIS and GIS conditions in Fig. 2. Upon a 633 nm lasing illumination, the typical four-stage dynamic behaviors are clearly observed under the three conditions in Fig. 2a, indicating a distinct pyro-phototronic photocurrent

response.[42] Notably, the p-n junction under the GIS condition displays the highest steady photovoltaic current and peak current, indicating a large enhancement of GIS in photocurrent response. For the heterojunction under the GIS condition, the transient peak current (I_t), steady current (I_s) and transient peak-to-peak current ($I_{tt'}$) first rapidly then slowly increase with increasing the illumination power density from 0.04 to 4.17 mW cm^{-2} (Fig. 2b and S7, supporting information). More importantly, the steady and transient photocurrents are always larger than the corresponding response of the junction under the IIS or LCIS condition. The corresponding enhancement factor of photocurrent induced by the GIS is defined as $\gamma_I = (I-I_0)/I_0$ relative to the case under the IIS or LCIS condition, where I is the peak-to-peak photocurrent $I_{tt'}$ or steady photocurrent I_s of the junction under the GIS condition, and I_0 represents the corresponding current of the junction under the IIS or LCIS condition. Relative to the initial heterojunction, the obtained enhancement factor γ_{IsI} in steady photocurrent is generally larger than the corresponding γ_{ItI} in transient photocurrent (Fig. 2c), demonstrating a stronger enhancement of GIS in photovoltaic effect through decreasing the IS concentration and introducing an IS concentration gradient. The corresponding maximal γ_{IsI} (γ_{ItI}) reaches about 286% (123%), manifesting a significant improvement role of GIS in steady and transient photocurrent for the p-Si/n-ZnO heterojunction. Relative to the junction under the LCIS condition, the enhancement factor γ_{IsL} (γ_{ItL}) can reach 43% (28%), indicating the improvement role of the IS concentration gradient in steady (transient) photocurrent. Importantly, the significant improvement of photoresponse of heterojunction with GIS condition relative to the junction with LCIS clearly demonstrates the modulation role of IS concentration gradient. The introduced GIS also improves the photocurrent response performances of the p-Si/n-ZnO heterojunction as a self-powered PD to UV lasing and near infrared (NIR) lasing (Fig. 2d), suggesting a broadband enhancement characteristic of the GIS. Additionally, the obtained heterojunction is only treated by a 0.19 V voltage as a comparison experiment. The photocurrent response displays a negligible variation for UV, visible and NIR detection in Fig. S8. This result reveals that the obtained GIS is attributed to the synergistic combination of external electric field-assisted UV irradiation as

designed, not the direct effects of field-induced polarization or field-induced IS distribution within ZnO.

The tuning regulation of IS concentration gradient is carefully illustrated in Fig. 3 through measuring the dynamic photocurrent and photovoltage responses of the p-Si/n-ZnO heterojunction treated by the electric field-assisted UV irradiation under varying external bias voltage U_{ex} and a fixing energy density W_{ir}. Given the role of the external electric field in generating GIS as analyzed above, IS concentration gradient ($\nabla\rho_{IS}$) increases with increasing U_{ZnO}, while the average IS concentration remains nearly constant due to the fixing W_{ir}, resulting in an almost constant electron concentration (Fig. 3a). Consequently, the simulated built-in electric field strengthens with increasing $\nabla\rho_{IS}$, highlighting the enhancement effect of the IS concentration gradient on built-in electric field of the p-n junction (Fig. 3a). The enhanced built-in electric field provides a stronger driving force for the separation and transportation of photon-generated carriers across the p-Si/n-ZnO heterojunction. As a result, both the 633 nm laser-generated photocurrent and photovoltage exhibit an increasing trend with the partial voltage U_{ZnO} (i.e. $\boldsymbol{E}_{tr}$) (Fig. 3b and 3c). The corresponding transient signal is always larger than the steady signal, demonstrating the enhancement role of pyro-phototronic effect on voltage and current. The measured built-in potential exhibits a rapid increase followed by saturation as shown in Fig. 3a through the C^{-2}-V curves of the junction treated under different U_{ZnO} (Fig. S9, supporting information). A similar phenomenon is also observed in the built-in field-controlled transient and stable photovoltage signals as they vary with U_{ZnO}, revealing a consistent inflection point at U_{ZnO} = 0.13 V (Fig. 3b and 3c). This phenomenon indicates that the built-in field and $\nabla\rho_{IS}$ first increase with U_{ZnO} when it is smaller than 0.13 V and then remain nearly constant when U_{ZnO} > 0.13 V. In contrast, the transient ($I_{tt'}$) and steady (I_s) photocurrents exhibit a monotonic increase with U_{ZnO} ranging from 0.0 V to 0.27 V. This monotonic behavior might be attributed to the combined effect of a reduction in interface resistance and the saturation of the built-in field when U_{ZnO} exceeds 0.13 V. Additionally, the pyroelectric improvement factor (β) of the transient photocurrent (photovoltage) relative to the steady photocurrent (photovoltage) is defined as $\beta_I = (I-I_s)/I_s$ ($\beta_V = (V-V_s)/V_s$), where I

denotes $I_{tt'}$ or I_t as shown in Fig. 3d. This demonstrates the significant enhancement of pyro-phototronic effect on photocurrent and photovoltage for the p-Si/n-ZnO heterojunction with different $\nabla\rho_{IS}$. This result suggests that IS concentration gradient can be flexibly adjusted to modulate the photoresponse of heterojunction by changing the external electric field intensity during the electric field-assisted UV irradiations. As U_{ZnO} increases, β_V initially shows a rapid decrease followed by saturation, while β_I shows a trend of rapid decrease, saturation, and subsequent increase. This behavior underscores the tuning influence of the IS concentration gradient on pyro-phototronic effect, thereby supplying a method to modulate the pyro-phototronic effect.

The tuning regulation of IS average concentration is also demonstrated through measuring the dynamic photocurrent and photovoltage responses of the p-Si/n-ZnO heterojunction through varying the UV irradiation energy density W_{ir} at a fixed treating bias voltage U_{ZnO}. With increasing irradiation energy density, the IS average concentration ρ_{IS} initially decreases rapidly, then decreases slowly until it reaches a relatively stable minimum value, while $\nabla\rho_{IS}$ first increases and then decreases due to most IS being removed by sufficient UV irradiation. Consequently, the simulated built-in electric field first increases and then slightly decreases with increasing W_{ir} (Fig. 4a). As a result, the photocurrent and photovoltage response to 633 nm lasing excitation both exhibit a typical pyro-phototronic behavior, showing an obvious enhancement in response performance with increasing irradiation energy density W_{ir} (Fig. 4b). The measured built-in potential of the treated junction displays a trend of initial increase, then saturation and slight decrease with increasing W_{ir} (Fig. 4a and Fig. S10, supporting information), showing two inflection points at 350 mJ cm^{-2} and 630 mJ cm^{-2}. The steady photocurrent and photovoltage responses to 633 nm lasing excitation display a similar trend of initial increase, saturation and slight decrease (Fig. 4c), consistent with the behavior of the built-in potential. In contrast, the corresponding transient photocurrent and photovoltage increase monotonically with W_{ir}, even when the built-in potential reaches its saturation value or begins to decrease. The rapid increase in the transient optoelectronic signal, despite the slight decrease in built-in potential, might be attributed to the significant enhancement of the pyro-phototronic effect due to the

reduction in IS concentration, which suppresses the screening effect of IS on polarization charges.[13] The corresponding pyroelectric improvement factor β_V first decreases, then remains constant, then increases, and finally slightly decreases as W_{ir} increases from 0 to 840 mJ cm^{-2} (Fig. 4d), showing the tunability of IS concentration distribution on the voltaic signal induced by the pyro-phototronic effect. Importantly, β_I first decreases, then remains constant, and finally increases rapidly with increasing W_{ir} (Fig. 4d), indicating the significant influence of IS concentration distribution on pyro-phototronic effect. When W_{ir} exceeds 700 mJ cm^{-2}, the pyroelectric improvement factor β_I increases sharply and reaches a large value of 2800%, showing a significant improvement of pyro-phototronic effect on current signal. This increase might be attributed to the decrease of average electron concentration (Fig. 4a), which allows more pyroelectric polarizing charges to be released.[61] These findings reveal the excellent modulation capability of both IS concentration and gradient on pyro-phototronic effect through adjusting the treated electric field and irradiation energy density.

Working mechanism of the GIS-improved PDs. The working mechanism of GIS-improved pyro-phototronic PD is schematically illustrated in Fig. 5a through revealing the tuning role of GIS on energy band and carrier transportation based on Anderson's model.[48] In a p-Si/n-ZnO heterojunction under the IIS condition, a built-in electric field is typically established within the depletion region, accompanied by the introduction of IS energy levels on the ZnO side (Fig. S11 (a1, a2)). After the junction is treated by the process of external field-assisted UV irradiation, the IS within ZnO nanofilm exhibits a nonuniform distribution from the interface to the surface. This GIS induces an additional electric field E_{GIS} aligned with the built-in electric field E_{bi} (Fig. S11 (b1, b2)) and results in a distinctly tilted energy band within ZnO film (Fig. 5a(iii)). Upon visible illumination, the combined electric field of E_{GIS} and E_{bi}, referred to as the equivalent built-in electric field, provides a larger driving force for the separation and transportation of photogenerated carrier. As a result, the introduction of GIS within the ZnO film effectively enhances the separation efficiency of photogenerated carriers, resulting in a notable improvement in the steady photocurrent and photovoltage of the

p-n junction. The tilted band structure facilitates carrier transportation through the ZnO film, thereby reducing the response time. Additionally, the IS gradient induces an additional polarization field aligned with the spontaneous polarization field within the ZnO, resulting from a slight breaking of symmetry as a secondary effect. This slightly enhances the total polarization field within the ZnO film. Consequently, the transient photocurrent $I_{tt'}$ and photovoltage $V_{tt'}$ are improved, though with a relatively small enhancement factor compared to the corresponding the steady signals (Fig. 3c and 4c). It should be pointed out that the existing multi-interface scattering in ZnO nanofilms caused by grain boundaries may lead to the relative weak temperature increase effect, thereby reducing the pyroelectric effect and weakening the enhancement role of the GIS on the transient photocurrent response.[62,63] Also, the difference in enhancement factors between a significant enhancement of the transient signal and a slight enhancement of the transient signal results in a significant modification role of pyro-phototronic effect on the optoelectric response.

The enhancement role of GIS on the self-powered PDs. The enhancement role of GIS on broadband performance of the PD is also evaluated through comparing the dynamic photocurrent response of the heterojunction under the IIS, LCIS and GIS conditions using a series of quasi-monochromatic beams (Fig. 5b, S12, supporting information). The *I-t* photocurrent response of the heterojunction under the GIS condition demonstrates a remarkable pyro-photoronic effect and an excellent optoelectric response within the UV-Vis-NIR range. Relative to the initial heterojunction under the IIS condition, the obtained enhancement factor γ_{IsI} in steady photocurrent is generally larger than the corresponding γ_{ItI} in transient photocurrent (Fig. 5c), demonstrating a strong enhanced photovoltaic effect by the GIS over the wavelength range from 320 nm to 1120 nm. The corresponding maximal γ_{IsI} (γ_{ItI}) reaches about 1540% (237%) under 840 nm photoexcitation, manifesting a significant steady and transient photocurrent improvement of GIS for the p-Si/n-ZnO heterojunction. Relative to the junction under the LCIS condition, the maximal enhancement factor γ_{IsL} (γ_{ItL}) is about 486% (154%), indicating the improvement of the IS concentration gradient in steady (transient) photocurrent. The improvement factor of

heterojunction with GIS on the steady photocurrent is always larger than that on the transient photocurrent. The significant difference may attribute to the remarkable equivalent built-in electric field enhancement induced by GIS within heterojunction and the relatively small light-induced temperature variation due to the multi-interface scattering caused by grain boundaries.[62, 63]

The key parameter responsivity (R) defined as $R = \frac{I_{\text{ligh}} - I_{\text{dark}}}{P_{\text{ill}}}$ is presented in Fig. 5d, where I_{light} and I_{dark} refer to short-circuit current with and without illumination, and P_{ill} is defined as the exciting power on the PD, respectively. The obtained transient responsivity $R_{\text{tt}'}$ is generally larger than the corresponding steady photoresponsivity R_{s}, which significantly exceeds the values of the reported ZnO-based self-powered PDs.[47, 64] This result demonstrates the improvement of pyro-phototronic effect in photoresponsivity of the p-Si/n-ZnO heterojunction under the GIS condition. Additionally, the impact of the GIS on the response time of the PD is further demonstrated by comparing the rise time and fall time of the heterojunction under the IIS, LCIS and GIS conditions (Fig. S13, supporting information). The rise (fall) time is defined as the time taken for the photocurrent to increase (decrease) from 10% (90%) to 90% (10%) of its maximum value. The rise time is reduced from 25 μs (IIS) to 20 μs, and the fall time is shortened from 75 μs (IIS) to 70 μs by the obtained GIS within the heterojunction. This reduction in response time indicates that the GIS is beneficial to fabricate self-power PDs with fast response capabilities.

The stability of the generated GIS state is uncovered through long-term measurements of the photocurrent response of the treated junction in both vacuum and air environment (Fig. S14, supporting information). The photocurrent response shows negligible variation in vacuum, indicating the excellent robustness of the generated GIS state under vacuum conditions. In contrast, a remarkable relaxation process is observed in air, highlighting the oxygen-dependent nature of the generated GIS.

Furthermore, the GIS generation method of electric field-assisted UV irradiation is extended to other oxide semiconductor heterostructures. For ZnO nanofilms prepared by magnetron sputtering (@1) and hydrothermal methods (@2), the formed p-Si/n-ZnO

heterojunctions under the GIS condition both demonstrate a significant improvement in photocurrent response to 633 nm lasing compared to those under IIS and LCIS conditions (Fig. S15a and S15b, supporting information). For the Al/p-Si/n-ZnO/ITO heterojunction (@3), the transient and stable photocurrents are enhanced by 357% and 614%, respectively, through introducing GIS within the ZnO film (Fig. S15c, supporting information). For the p-Si/n-ZnO heterojunction based on Ga-doped ZnO film (@4), the GIS within the ZnO film significantly improves both the steady and transient photocurrent compared to the junction under the IIS condition (Fig. S15d, supporting information). Moreover, the photocurrent of the heterojunction with GIS is consistently higher than that under the LCIS condition, indicating the enhancement role of the IS concentration gradient for the oxide-based heterojunctions. These results confirm that the proposed GIS generation method and its photoelectric response enhancement effect are universally applicable to oxide-based p-n junctions. This method provides a flexible and effective approach for designing and optimizing high-performance oxide semiconductor-based photoelectric conversion devices. It should be pointed out that the different enhancement effects exhibited by various heterojunctions may be attributed to the variations of initial IS distribution in the heterojunctions with different ZnO film quality and electrode type, which may significantly affect the modulation effect of the electric field-assisted UV irradiation on the vertical distribution of the IS in oxide-based heterostructures.

Conclusions and discussions

In this study, we have demonstrated a groundbreaking approach to dynamically manipulate the once-discarded IS with random distribution in oxides. The designed IS distribution significantly improves the photoelectric response performance of the self-powered PDs. The fabricated oxide-based heterojunction with GIS exhibits novel, unique, and upcycled features compared to conventional self-powered PDs. This proposed design principle and modification methodology represent a paradigm shift in reusing long-term discarded IS distribution. First, the introduced GIS, tailored by external electric field-assisted UV irradiation, effectively modulates the pyro-phototronic effect. This mechanism fundamentally differs from directly removing IS,

instead transforming waste into treasure by utilizing the naturally occurring IS within ZnO nanocrystal grains. The heterojunction under the GIS condition demonstrates a lower interface transfer resistance compared to the junction with random-distribution ISs. The designed GIS significantly enhances the equivalent built-in electric field and transient photoresponse performance, showcasing a dynamic modulation behavior of the pyro-phototronic effect through tailoring IS distribution. Second, the approach of generating different GIS conditions is more environmentally friendly and practical. The IS distribution can be flexibly adjusted by manipulating the treating electric field and irradiation energy density for ZnO-based PDs. This method is also applicable to other oxide semiconductor films, including various ZnO films fabricated by different methods and Ga-doped ZnO films, thereby broadening the material range for more practical applications. Third, the heterojunction under the GIS condition as a self-powered PD exhibits a remarkable improvement in steady (transient) photoresponsivity across a broad wavelength range of 320-1120 nm. Notably, the enhancement factor reaches an impressive 1540% (237%) compared to the initial junction. This significant enhancement underscores the potential of GIS in promoting the performance of self-powered PDs. Our findings pave the way for further exploration the function of IS distributions in enhancing the performances of self-powered PDs, offering a promising avenue for future development and applications of the oxide semiconductor in photodetection technology.

Methods

Device preparation. The p-type Si (100) wafer with a resistivity of 1-20 Ω cm and 500 μm thickness was washed away floating dust by deionized water and alcohol respectively, and then was etched by mixed solution of 0.3 wt% NaOH and 8% isopropanol to remove the oxidation layer for further usage. The ZnO film was prepared by sol-gel method. Firstly, zinc acetate dihydrate ($Zn(CH_3COO)_2 \cdot 2H_2O$) was dissolved in ethanol using ethane-diamine and mono-ethanolamine as stabilizer, afterwards was stirred at 50 ℃ for 30 min, and then was left at room temperature for 48 h to get ZnO precursor solution. The obtained ZnO precursor was spin-coated on the prepared silicon

wafer, and then annealing at 600 ℃ for 2 h to form ZnO film. Finally, the 150 nm-thickness ITO layers were deposited on the ZnO film and Si substrate as the top and bottom electrodes by employing radio frequency magnetron sputtering (PVD75, Kurt. J. Lesker Company) at power of 150 W for 15 min.

Device treating. The fabricated p-n heterojunctions were treated by only UV irradiation and external-field assisted UV irradiation to obtain the devices under the conditions of LCIS and GIS before photon detecting, respectively. A UV objective was utilized to expand 325 nm lasing to irradiate the whole device. The synthesized function generator (DS345, Stanford) was employed to supply the external DC bias voltage on the p-n junction during the treating process of external-field assisted UV irradiation. During the treating process, the irradiation energy density is controlled by changing the irradiation period at a fixing irradiation power density of 7.0 mW cm^{-2}. Unless otherwise specified, the bias voltage was set at 1.0 V and the UV irradiation energy density was 210 mJ cm^{-2}.

Characteristics and measurements. The morphology of ZnO film were characterized by scanning electron microscope (SEM) (SU8010, Hitachi). Photoluminescence spectra of the prepared ZnO nanofilm was tested by using a fluorescence spectrometer (Fluorolog-Tau-3) with an excitation 325 nm laser (Model No. IK5751I-G, Kimmon Koha Co., Ltd.). Absorption spectra of the ZnO nanofilm was obtained by an Ultraviolet-visible Spectrophotometer (LAMBDA950, PE). AC Impedance of the p-n heterojunctions were characterized by an electrochemical workstation (Chi660e, Chinstruments). *I-V* and *C-V* curves of the obtained p-n junctions were measured using Keithley 4200A semiconductor analyzer (4200A-SCS, Ketithley). The input photon stimuli were provided by the He-Cd dual-color laser (Model No. IK5751IG, Kimmon Koha Co., Ltd.), 633 nm solid-state laser (25-LHP-928-230), and 1064 nm semiconductor laser (LDC-3706, Newport). A flexibly tunable quasi-monochromatic light source was also home-made as various illuminations with the central wavelength in the range of 320-1120 nm covering UV-Vis-NIR range at a power density of 5 μW cm^{-2} based on a Xe lamp and grating spectrometer (ARC-SP-2155, Princeton Instruments). A continuously variable neutral attenuator was employed

to control the power density of the optical stimuli. The light power density was measured by optical-power meter (PM320E, Thorlabs). The *I-t* and *V-t* curves were measured by a home-made computer-controlled measurement system with a Stanford SRS low noise current preamplifier (SR570, Stanford)/SRS low noise voltage preamplifier (SR560, Stanford) in conjunction with a GPIB controller (GPIB-USB-HS, NI 488.2). The transient photon current and voltage response of the p-n junctions were measured at a zero bias at different illuminations with different wavelength and different power density as a self-powered photodetector.

Simulations. The electric property of the p-Si/n-ZnO heterojunctions with different IS distributions were simulated by the semiconductor module of finite element method. In simulations, a simple physical model was adopted to uncover the tuning role of IS distribution on the junction electric field, potential and band structure through considering the electron concentration variations induced by the IS and induced charge distribution induced by IS concentration gradient within ZnO side. The p-Si/n-ZnO heterojunction consists of 1 μm Si layer and 100 nm ZnO layer. The acceptor doping concentration (1-20 Ω cm), relative permittivity, electron affinity and band gap of Si are set as 6.25×10^{20} m^{-3}, 11.7, 4.05 eV and 1.12 eV, respectively. The relative permittivity, electron affinity and band gap of ZnO are assumed as 8.5, 4.35 eV and 3.37 eV. [48] The electron concentrations of ZnO nanofilms are set as 1.6×10^{17} m^{-3} for the IIS condition, 1.66×10^{17} m^{-3} for the LCIS condition and 1.67×10^{17} m^{-3} for the GIS condition according to the measurement results from C^{-2}-V curves. For the p-n junction with GIS in ZnO nanofilm, a negative space charge density of ρ_q = 100 C m^{-3} were introduced within the ZnO layer to demonstrate the IS gradient effect. And a positive charge sheet density of $\rho_s = 1\times10^{-5}$ C m^{-2} at the surface of ZnO were introduced for electrical neutrality.

Supporting Information

Supporting Information is available from the Wiley Online Library or from the author.

Acknowledgments

The authors acknowledge financial support by International science and technology cooperation projects commissioned by Beijing Municipal Science and Technology Commission (Grant no. Z221100002722019) and the National Natural Science Foundation of China (Grant Nos. 61975018 and 921501109).

Authorship contributions

Meng Zhu: Conceptualization, Methodology, Software, Data curation, Writing-original draft. **Xianchun Qiu:** Software, Methodology. **Jiayao Liu:** Data curation, Methodology. **Qing Chang:** Methodology. **Zhaona Wang:** Investigation, Methodology, Conceptualization, Supervision, Writing-review & editing, Project administration. **Zhong Lin Wang:** Supervision, Writing-review & editing. All authors discussed the results and reviewed the manuscript.

Conflict of Interest

The authors declare no conflict of interest.

Data Availability Statement

The authors declare that the data that support the findings of this study are available within the article and its Supplementary Information files. All other relevant data are available from the corresponding authors upon request.

References

[1] C. Jia, S. Wu, J. Fan, C. Luo, M. Fan, M. Li, L. He, Y. Yang, H. Zhang. Ferroelectrically Modulated and Enhanced Photoresponse in a Self-Powered α-In_2Se_3/Si Heterojunction Photodetector. *ACS Nano* **17**, 6534-6544 (2023).

[2] L. Lin, Y. Liu, W. Wu, L. Huang, X. Zhu, Y. Xie, H. Liu, B. Zheng, J. Liang, X. Sun, C. Zhu, G. Wu, Q. Shuai, Z. Huang, T. Wang, D. Li, A. Pan. Self‐Powered Perovskite Photodetector Arrays with Asymmetric Contacts for Imaging Applications. *Adv. Electron. Mater.* **9**, 2300106 (2023).

[3] Y. Miao, J. Wu, X. Qi, L. Yang, X. Wang, F. Zheng, F. Zhao, S. Shafique, Y. Zhu, Z. Hu. Gradient 2D-3D Ruddlesden-Popper perovskite film for high-performance self-powered photodetectors. *Nano Energy* **113**, 108605 (2023).

[4] L. Hu, J. Yan, M. Liao, H. Xiang, X. Gong, L. Zhang, X. Fang. An Optimized Ultraviolet-A Light Photodetector with Wide-Range Photoresponse Based on ZnS/ZnO Biaxial Nanobelt. *Adv. Mater.* **24**, 2305-2309 (2012).

[5] S. M. Hatch, J. Briscoe, S. Dunn. A Self-Powered ZnO-Nanorod/CuSCN UV Photodetector Exhibiting Rapid Response. *Adv. Mater.* **25**, 867-871 (2013).

[6] X. Liu, L. Gu, Q. Zhang, J. Wu, Y. Long, Z. Fan. All-printable band-edge modulated ZnO nanowire photodetectors with ultra-high detectivity. *Nat. Commun.* **5**, 4007 (2014).

[7] B. Zhao, F. Wang, H. Chen, L. Zheng, L. Su, D. Zhao, X. Fang. An Ultrahigh Responsivity (9.7 mA W^{-1}) Self-Powered Solar-Blind Photodetector Based on Individual ZnO-Ga_2O_3 Heterostructures. *Adv. Funct. Mater.* **27**, 123504 (2017).

[8] Y. Ning, Z. Zhang, F. Teng, X. Fang. Novel Transparent and Self-Powered UV Photodetector Based on Crossed ZnO Nanofiber Array Homojunction. *Small* **14**, 1703754 (2018).

[9] W. Ouyang, J. Chen, Z. Shi, X. Fang. Self-powered UV photodetectors based on ZnO nanomaterials. *Applied Physics Reviews* **8**, 031315 (2021).

[10] Y. Peng, J. Lu, X. Wang, W. Ma, M. Que, Q. Chen, F. Li, X. Liu, W. Gao, C. Pan. Self-powered high-performance flexible GaN/ZnO heterostructure UV photodetectors with piezo-phototronic effect enhanced photoresponse. *Nano Energy* **94**, 106945 (2022).

[11] J. D. Hwang, D. H. Wu, S. B. Hwang. Inserting an i-ZnO layer to increase the performance of p-Si/n-ZnO heterojunction photodetectors. *Mat. Sci. Semicon. Proc* **39**, 132-135 (2015).

[12] T. H. Flemban, M. A. Hague, I. Ajia, N. Alwadai, S. Mitra, T. Wu, I. S. Roqan. A Photodetector Based on p-Si/n-ZnO Nanotube Heterojunctions with High Ultraviolet Responsivity. *ACS Appl. Mater. Interfaces* **9**, 37120-37127 (2017).

[13] Y. Zhang, M. Hu, Z. Wang. Enhanced performances of p-si/n-ZnO self-powered photodetector by interface state modification and pyro-phototronic effect. *Nano Energy* **71**, 104630 (2020).

[14] A. A. Ahmed, T. F. Qahtan, M. R. Hashim, A. T. Nomaan, N. H. Al-Hardan, M. Rashid. Eco-friendly ultrafast self-powered p-Si/n-ZnO photodetector enhanced by photovoltaic-pyroelectric coupling effect. *Ceram. Int.* **48**, 16142-16155 (2022).

[15] M. Xue, W. Peng, X. Tang, Y. Cai, F. Li, Y. He. Pyro-Phototronic Effect Enhanced Pyramid Structured p-Si/n-ZnO Nanowires Heterojunction Photodetector. *ACS Appl. Mater. Interfaces* **15**, 4677-4689 (2023).

[16] S. Cho, J.-W. Jang, H. J. Park, D.-W. Jung, A. Jung, J. S. Lee, K.-H. Lee. A method for synthesizing ZnO-carbonaceous species nanocomposites, and their conversion to quasi-single crystal mesoporous ZnO nanostructures. *Rsc Adv.* **2**, 566-572 (2012).

[17] E. Kim, Y. Vaynzof, A. Sepe, S. Guldin, M. Scherer, P. Cunha, S. V. Roth, U. Steiner. Gyroid-Structured 3D ZnO Networks Made by Atomic Layer Deposition. *Adv. Funct. Mater.* **24**, 863-872 (2014).

[18] J. C. D. Faria, A. J. Campbell, M. A. McLachlan. ZnO Nanorod Arrays as Electron Injection Layers for Efficient Organic Light Emitting Diodes. *Adv. Funct. Mater.* **25**, 4657-4663 (2015).

[19] Q. C. Bui, G. Ardila, E. Sarigiannidou, H. Roussel, C. Jimenez, O. Chaix-Pluchery, Y. Guerfi, F. Bassani, F. Donatini, X. Mescot, B. Salem, V. Consonni. Morphology Transition of ZnO from Thin Film to Nanowires on Silicon and its Correlated Enhanced Zinc Polarity Uniformity and Piezoelectric Responses. *ACS Appl. Mater. Interfaces* **12**, 29583-29593 (2020).

[20] V. Etacheri, R. Roshan, V. Kumar. Mg-Doped ZnO Nanoparticles for Efficient Sunlight-Driven Photocatalysis. *ACS Appl. Mater. Interfaces* **4**, 2717-2725 (2012).

[21] S. Muthukumaran, R. Gopalakrishnan. Structural, FTIR and photoluminescence studies of Cu doped ZnO nanopowders by co-precipitation method. *Opt. Mater.* **34**, 1946-1953 (2012).

[22] W. Yu, J. Zhang, T. Peng. New insight into the enhanced photocatalytic activity of N-, C- and S-doped ZnO photocatalysts. *Appl. Catal. B* **181**, 220-227 (2016).

[23] W.-C. Lin, P.-C. Chang, C.-J. Tsai, T.-C. Hsieh, F.-Y. Lo. Magnetism modulation of Fe/ZnO heterostructure by interface oxidation. *Appl. Phys. Lett.* **103**, 212405 (2013).

[24] Z. Guo, L. Zhou, Y. Tang, L. Li, Z. Zhang, H. Yang, H. Ma, A. Nathan, D. Zhao. Surface/Interface Carrier-Transport Modulation for Constructing Photon-Alternative Ultraviolet Detectors Based on Self-Bending-Assembled ZnO Nanowires. *ACS Appl. Mater. Interfaces* **9**, 31042-31053 (2017).

[25] Z. Kang, H. Si, S. Zhang, J. Wu, Y. Sun, Q. Liao, Z. Zhang, Y. Zhang. Interface Engineering for Modulation of Charge Carrier Behavior in ZnO Photoelectrochemical Water Splitting. *Adv. Funct. Mater.* **29**, 1808032 (2019).

[26] C. J. Park, J. W. Kim, S. D. Namgung, J.-Y. Kwon, M. W. Shin. Selective photo -thermal modulation of ZnO/Pt interface for monolithic 3D integration of oxide -based resistive random access memory. *Appl. Surf. Sci.* **520**, 146380 (2020).

[27] Z. Xu, Y. Zhang, Z. Wang. ZnO-based photodetector: from photon detector to pyro-phototronic effect enhanced detector. *J. Phys. D: Appl. Phys.* **52**, 223001 (2019).

[28] V. Panwar, S. Nandi, M. Majumder, A. Misra. Self-powered ZnO-based pyro-phototronic photodetectors: impact of heterointerfaces and parametric studies. *Journal of Materials Chemistry C* **10**, 12487-12510 (2022).

[29] S. Sahare, P. Ghoderao, M. K. Sharma, M. Solovan, R. Aepuru, M. Kumar, Y. Chan, M. Ziółek, S.-L. Lee, Z.-H. Lin. Pyro-phototronic effect: An effective route toward self-powered photodetection. *Nano Energy* **107**, 108172 (2023).

[30] J. Tian. An overview of pyroelectric photodetector: Photoresponse mechanisms and applications. *AIP Advances* **13**, 050701 (2023).

[31] Z. Chen, B. Li, X. Mo, S. Li, J. Wen, H. Lei, Z. Zhu, G. Yang, P. Gui, F. Yao, G. Fang. Self-powered narrowband p-NiO/n-ZnO nanowire ultraviolet photodetector with interface modification of Al_2O_3. *Appl. Phys. Lett.* **110**, 123504 (2017).

[32] Y. Wang, P. Wang, Y. Zhu, J. Gao, F. Gong, Q. Li, R. Xie, F. Wu, D. Wang, J. Yang, Z. Fan, X. Wang, W. Hu. High performance charge-transfer induced homojunction photodetector based on ultrathin ZnO nanosheet. *Appl. Phys. Lett.* **114**, 011103 (2019).

[33] F. Gunkel, D. V. Christensen, Y. Z. Chen, N. Pryds. Oxygen vacancies: The (in)visible friend of oxide electronics. *Appl. Phys. Lett.* **116**, 120505 (2020).

[34] Z. Wang, R. Lin, Y. Huo, H. Li, L. Wang. Formation, Detection, and Function of Oxygen Vacancy in Metal Oxides for Solar Energy Conversion. *Adv. Funct. Mater.* **32**, 2109503 (2021).

[35] Y. Zhu, S. Lin, W. Gao, M. Zhang, C. Yang, P. Feng, C. Xu, Z. L. Wang. Effects of Oxygen Vacancies and Cation Valence States on the Triboelectric Property of Substoichiometric Oxide Films. *ACS Appl. Mater. Interfaces* **13**, 35795-35803 (2021).

[36] R. Chen, Z. Ren, Y. Liang, G. Zhang, T. Dittrich, R. Liu, Y. Liu, Y. Zhao, S. Pang, H. An, C. Ni, P. Zhou, K. Han, F. Fan, C. Li. Spatiotemporal imaging of charge transfer in photocatalyst particles. *Nature* **610**, 296-301 (2022).

[37] S. Kattel, P. J. Ramirez, J. G. Chen, J. A. Rodriguez, P. Liu. Active sites for CO_2 hydrogenation to methanol on Cu/ZnO catalysts. *Science* **355**, 1296-1299 (2017).

[38] J. Cao, B. Wu, R. Chen, Y. Wu, Y. Hui, B.-W. Mao, N. Zheng. Efficient, Hysteresis-Free, and Stable Perovskite Solar Cells with ZnO as Electron-Transport Layer: Effect of Surface Passivation. *Adv. Mater.* **30**, 1705596 (2018).

[39] J. M. Yuk, J. Y. Lee, Y. S. No, T. W. Kim, W. K. Choi. Formation mechanisms of ZnO amorphous layers due to thermal treatment of ZnO thin films grown on p-InP (100) substrates. *J. Appl. Phys.* **103**, 083535 (2008).

[40] H.-C. Fang, J.-H. Huang, W.-H. Chu, C.-P. Liu. Ga^+ focused-ion-beam implantation-induced masking for H_2 etching of ZnO films. *Nanotechnology* **21**, 505703 (2010).

[41] Z. Pan, W. Peng, F. Li, Y. He. Piezo‐Phototronic Effect on Performance Enhancement of Anisotype and Isotype Heterojunction Photodiodes. *Adv. Funct. Mater.* **28**, 1706897 (2018).

[42] Z. Wang, R. Yu, C. Pan, Z. Li, J. Yang, F. Yi, Z. L. Wang. Light-induced pyroelectric effect as an effective approach for ultrafast ultraviolet nanosensing. *Nat Commun* **6**, 8401 (2015).

[43] X. Han, M. X. Chen, C. F. Pan, Z. L. Wang. Progress in piezo-phototronic effect enhanced photodetectors. *J Mater Chem C* **4**, 11341-11354 (2016).

[44] W. Peng, R. Yu, X. Wang, Z. Wang, H. Zou, Y. He, Z. L. Wang. Temperature dependence of pyro-phototronic effect on self-powered ZnO/perovskite heterostructured photodetectors. *Nano Res.* **9**, 3695-3704 (2016).

[45] W. Peng, X. Wang, R. Yu, Y. Dai, H. Zou, A. C. Wang, Y. He, Z. L. Wang. Enhanced Performance of a Self‐Powered Organic/Inorganic Photodetector by Pyro‐Phototronic and Piezo‐Phototronic Effects. *Adv. Mater.* **29**, 1606698 (2017).

[46] M. Kumar, M. Patel, J. Kim, D. Lim. Enhanced broadband photoresponse of a self-powered photodetector based on vertically grown SnS layers via the pyro-phototronic effect. *Nanoscale* **9**, 19201-19208 (2017).

[47] S. Qiao, H. Sun, J. Liu, G. Fu, S. Wang. The nanowire length dependence of the photoresponse and Pyro-phototronic response in the ZnO-based heterojunctions. *Nano Energy* **95**, 107004 (2022).

[48] L. J. Guo, X. Liu, R. D. Cong, L. J. Gao, K. Zhang, L. Zhao, X. Z. Wang, R. N. Wang, C. F. Pan, Z. Yang. Patterned 2D Ferroelectric Perovskite Single-Crystal Arrays for Self- Powered UV Photodetector Boosted by Combining Ferro-Pyro- Phototronic and Piezo-Phototronic Effects. *Nano Lett* **22**, 8241-8249 (2022).

[49] P. Wan, M. Jiang, T. Xu, Y. Liu, X. Fang, C. Kan. Doping Concentration Influenced Pyro-Phototronic Effect in Self-Powered Photodetector Based on Ga-Incorporated ZnO Microwire/p^+-GaN Heterojunction. *Adv. Opt. Mater.* **10**, 2101851 (2022).

[50] S. Podder, B. Basumatary, D. Gogoi, J. Bora, A. R. Pal. Pyro-phototronic application in the Au/ZnO interface for the fabrication of a highly responsive ultrafast UV photodetector. *Appl. Surf. Sci.* **537**, 147893 (2021).

[51] J. Dong, Z. Wang, X. Wang, Z. L. Wang. Temperature dependence of the pyro-phototronic effect in self-powered p-Si/n-ZnO nanowires heterojuncted ultraviolet sensors. *Nano Today* **29**, 100798 (2019).

[52] Y. Feng, Y. Zhang, Y. Wang, Z. Wang. Frequency response characteristics of pyroelectric effect in p-n junction UV detectors. *Nano Energy* **54**, 429-436 (2018).

[53] Y. Zhu, B. Wang, C. Deng, Y. Wang, X. Wang. Photothermal-pyroelectric-plasmonic coupling for high performance and tunable band-selective photodetector. *Nano Energy* **83**, 105801 (2021).

[54] Q. Li, J. Huang, J. Meng, Z. Li. Enhanced Performance of a Self‐Powered ZnO Photodetector by Coupling LSPR‐Inspired Pyro‐Phototronic Effect and Piezo‐Phototronic Effect. *Adv. Opt. Mater.* **10**, 2102468 (2022).

[55] J. Simon, V. Protasenko, C. Lian, H. Xing, D. Jena. Polarization-Induced Hole Doping in Wide-Band-Gap Uniaxial Semiconductor Heterostructures. *Science* **327**, 60-64 (2010).

[56] X. Cai, L. Mao, S. Yang, K. Han, J. Zhang. Ultrafast Charge Separation for Full Solar Spectrum-Activated Photocatalytic H_2 Generation in a Black Phosphorus-Au-CdS Heterostructure. *ACS Energy Letters* **3**, 932-939 (2018).

[57] B. Qiu, Z. Chen, S. Qin, J. Yao, W. Huang, L. Meng, H. Zhu, Y. M. Yang, Z. G. Zhang, Y. Li. Highly Efficient All-Small-Molecule Organic Solar Cells with Appropriate Active Layer Morphology by Side Chain Engineering of Donor Molecules and Thermal Annealing. *Adv. Mater.* **32**, 1908373 (2020).

[58] L. Min, H. Sun, L. Guo, Y. Zhou, M. Wang, F. Cao, L. Li. Pyroelectric-Accelerated Perovskite Photodetector for Picosecond Light Detection and Ranging. *Adv. Mater.* **36**, 2400279 (2024).

[59] J. P. Donnelly, A. G. Milnes. The capacitance of p-n heterojunctions including the effects of interface states. *IEEE Trans. Electron. Dev* **14**, 63-68 (1967).

[60] E. S. Yang. Formation of interface states and defects in GaAs–$Al_xGa_{1-x}As$ DH lasers under room-temperature cw operation. *J. Appl. Phys.* **45**, 3801-3805 (1974).

[61] Z. Pan, W. Peng, F. Li, Y. He. Carrier concentration-dependent piezotronic and piezo-phototronic effects in ZnO thin-film transistor. *Nano Energy* **49**, 529-537 (2018).

[62] J. J. Kuo, M. Wood, T. J. Slade, M. G. Kanatzidis, G. J. Snyder. Systematic over-estimation of lattice thermal conductivity in materials with electrically-resistive grain boundaries. *Energy & Environmental Science* **13**, 1250-1258 (2020).

[63] P. Xu, W. Zhao, X. Liu, B. Jia, J. He, L. Fu, B. Xu. Dramatic Enhancement of Thermoelectric Performance in PbTe by Unconventional Grain Shrinking in the Sintering Process. *Adv. Mater.* **34**, 2202949 (2022).

[64] Q. Li, J. Meng, J. Huang, Z. Li. Plasmon‐Induced Pyro‐Phototronic Effect Enhancement in Self‐Powered UV-Vis Detection with a ZnO/CuO p-n Junction Device. *Adv. Funct. Mater.* **32**, 2108903 (2021).

Figure Captions

Figure 1

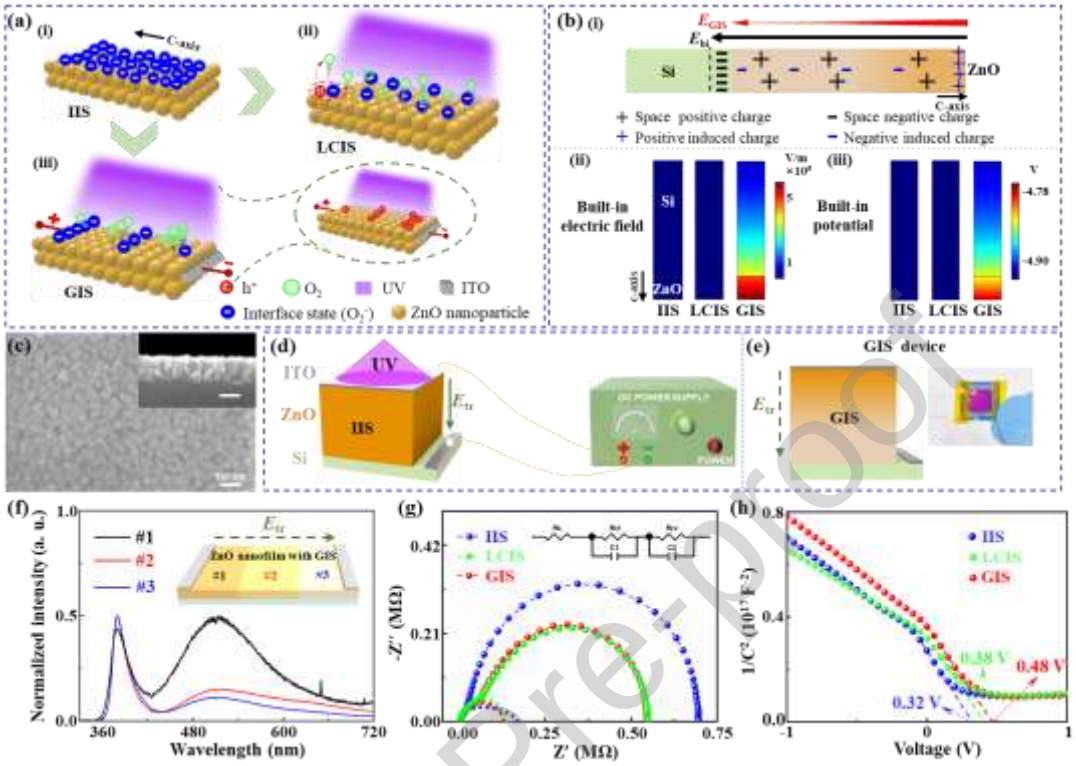

Fig. 1. Design and characterization of p-Si/n-ZnO heterojunction with GIS. (a) Schematic diagram of tailoring IS distribution in ZnO nanofilm. **(b)** Schematic diagram of electric filed distribution within p-Si/n-ZnO junction with GIS (i), and equivalent build-in electric filed (ii) and potential (iii) distribution within the junction with IIS, LCIS and GIS. **(c)** Scanning electron microscopy (SEM) images of ZnO nanofilm captured in top view and side view(inset). **(d)** Generation method of the GIS within p-Si/n-ZnO PD. **(e)** The obtained p-Si/n-ZnO PD with GIS (left) and its optical photograph (right). **(f)** Photoluminescence spectra of ZnO film with lateral GIS at different regions. **(g)** Nyquist plots of the junction under IIS, LCIS and GIS conditions with the inserted equivalent circuit model. **(h)** Capacitance as a function of bias voltage on the junction with IIS, LCIS and GIS.

Figure 2

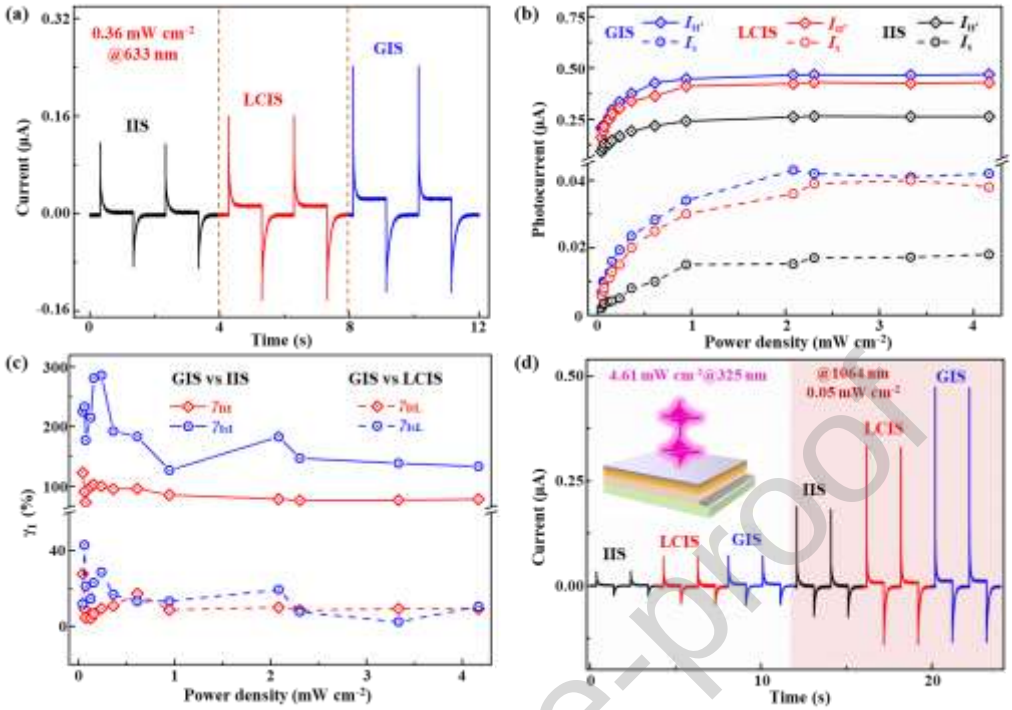

Fig. 2. Enhancement role of GIS in photoelectric response of p-Si/n-ZnO heterojunction as a self-powered PD. (a) *I-t* curves of the PD with IIS, LCIS and GIS under 633 nm lasing illumination at a power density of 0.36 mW cm^{-2}. **(b)** Photocurrent responses of the junction with IIS, LCIS and GIS varies with the exciting power density. **(c)** The enhancement factor of photocurrent by GIS varies with power density relative to that of the PD with IIS (γ_I) or LCIS (γ_{IL}). **(d)** *I-t* characteristics of the PD with IIS, LCIS and GIS under 325 nm (left) and 1064 nm (right) lasing illuminations.

Figure 3

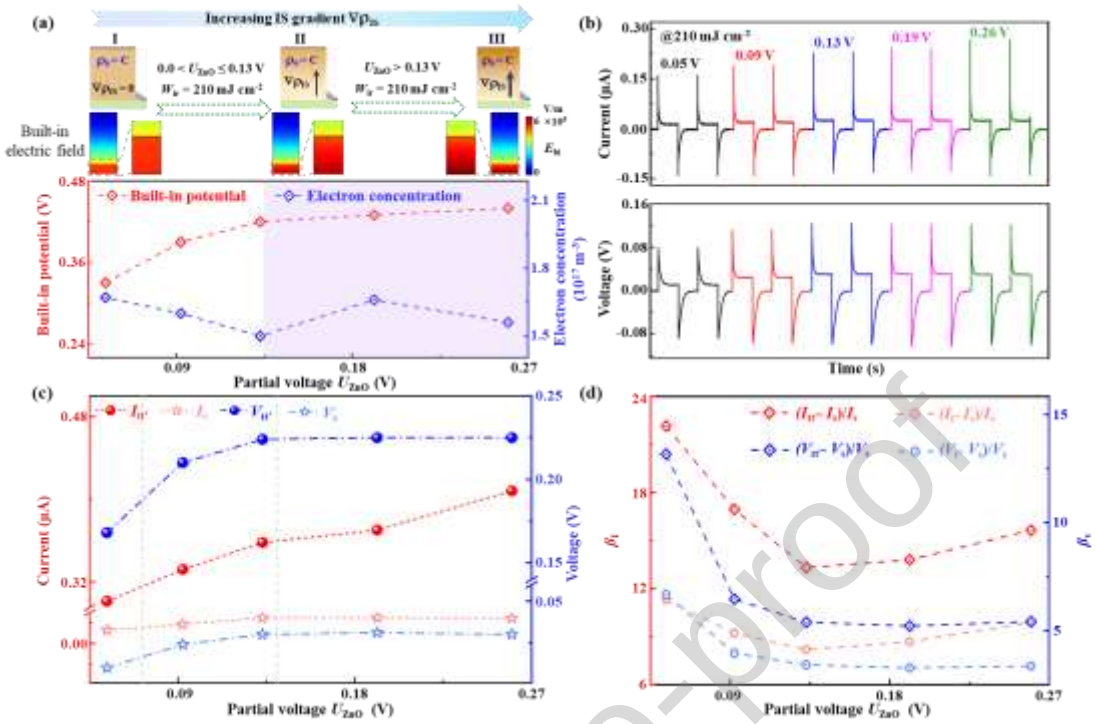

Fig. 3. Effect of IS gradient on photoelectric response of the PD. (a) Modification role of treating electric field on IS gradient and the simulated equivalent electric filed of the junction with different IS gradient (top); the measured equivalent built-in potential and electron concentration in ZnO film of p-Si/n-ZnO with different IS gradient. **(b)** *I-t* and *V-t* response curves of the PD treated by different treating field and a UV irradiation energy density of 210 mJ cm^{-2} for 633 nm lasing sensing at a power density of 0.36 mW cm^{-2}. **(c)** The corresponding $I_{tt'}$, I_s and $V_{tt'}$, V_s vary with the treating field. **(d)** Improvement factors of pyro-phototronic effect in photocurrent and photovoltage of the PD vary with the treating field.

Figure 4.

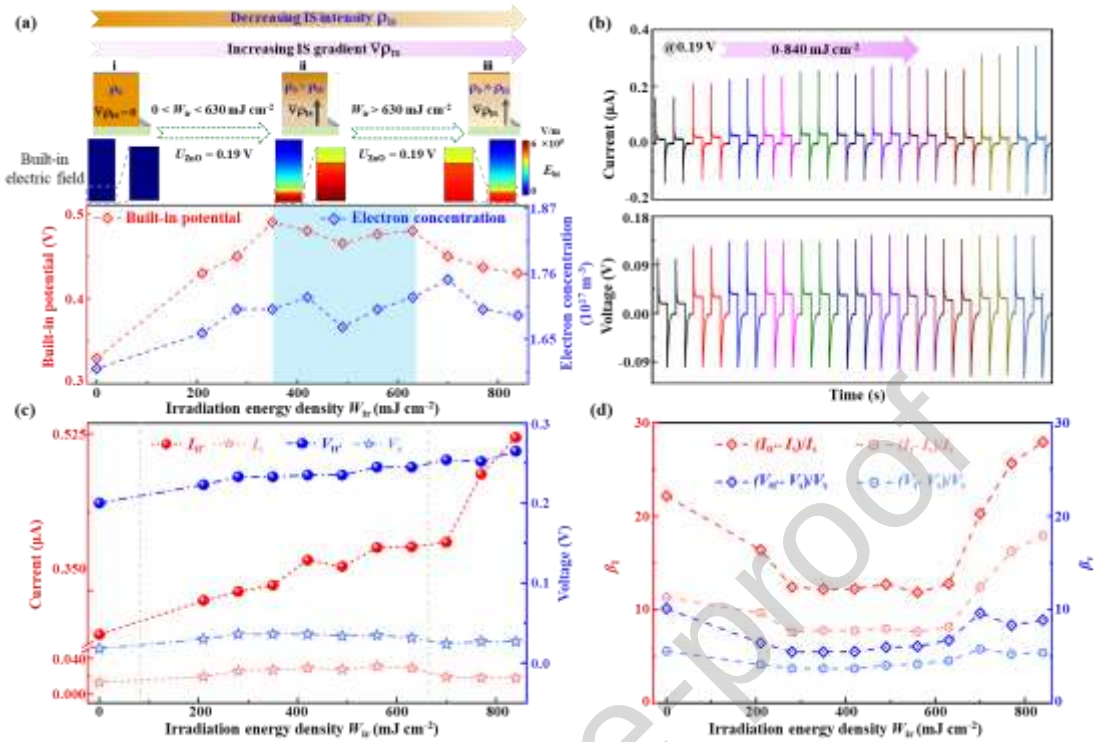

Fig. 4. Modulation effect of different GIS distribution on photoelectric response of the PD. **(a)** Modification role of UV irradiation on IS gradient and concentration within ZnO film at a fixing treating field U_{ZnO} = 0.19 V, the simulated equivalent electric filed of the junction (top); the measured equivalent built-in potential and electron concentration in ZnO film of p-Si/n-ZnO with different IS concentration and gradient. **(b)** *I-t* and *V-t* response curves of the PD treated at different UV irradiation energy densities and a fixing treating field U_{ZnO} = 0.19 V to a 633 nm lasing with a power density of 0.36 mW cm^{-2}. **(c)** The corresponding $I_{tt'}$, I_s and $V_{tt'}$, V_s vary with UV irradiation energy density. **(d)** Improvement factors of pyro-phototronic effect in photocurrent and photovoltage of the PD vary with the irradiation energy density.

Figure 5.

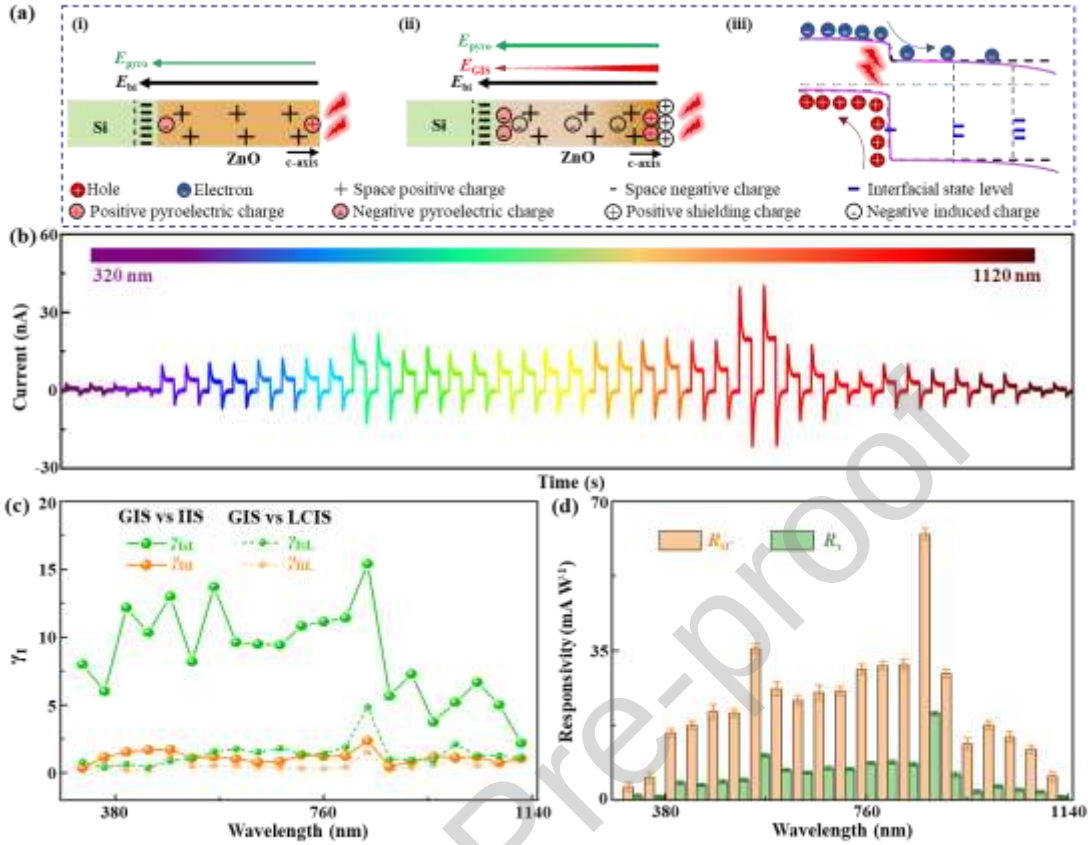

Fig. 5. Working mechanism and broad band performance of the p-Si/n-ZnO self-powered PD with GIS. (a) Distribution of charge, IS, electric filed and energy band diagrams of the p-Si/n-ZnO heterojunction with IIS and GIS upon visible illumination. **(b)** *I-t* curves of the p-Si/n-ZnO PD with GIS under various of quasi-monochromatic illuminations with peak wavelength within 320-1120 nm at a power density of 5 μW cm^{-2}. **(c)** The corresponding enhancement factors of steady and transient photocurrents by GIS vary with the peak wavelength of quasi-monochromatic illuminations. **(d)** Photoresponsivity of the fabricated PD with the GIS vary with the peak wavelength of quasi-monochromatic illuminations.

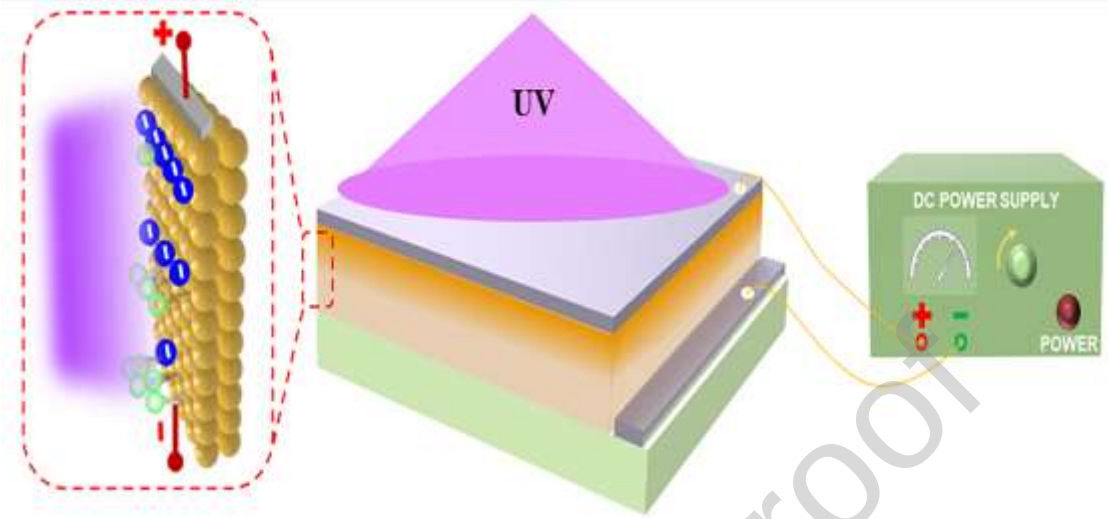

Declaration of Competing Interest

The authors declare no conflict of interest.

Highlights

- The GIS distribution is electrically manipulated and extendable to an oxide film.
- The GIS significantly enhances photocurrent of the oxide-based heterojunction.
- The self-powered PD with GIS has outstanding performances for UV-NIR waves.